

Neutron interferometric measurement of the scattering length difference between the triplet and singlet states of n-³He

M. G. Huber,* M. Arif, W. C. Chen,[†] T. R. Gentile, and D. S. Hussey
National Institute of Standards and Technology, Gaithersburg, MD 20899, USA

T. C. Black
University of North Carolina-Wilmington, Wilmington, NC 28403, USA

D. A. Pushin[‡]
University of Waterloo, Waterloo, ON N2L 3G1, Canada

C. B. Shahi and F. E. Wietfeldt
Tulane University, New Orleans, LA 70188, USA

L. Yang
University of Illinois at Urbana-Champaign, Urbana, IL 61801, USA
(Dated: November 27, 2021)

We report a determination of the n-³He scattering length difference $\Delta b' = b'_1 - b'_0 = (-5.411 \pm 0.031 \text{ (statistical)} \pm 0.039 \text{ (systematic)}) \text{ fm}$ between the triplet and singlet states using a neutron interferometer. This revises our previous result $\Delta b' = (-5.610 \pm 0.027 \text{ (statistical)} \pm 0.032 \text{ (systematic)}) \text{ fm}$ obtained using the same technique in 2008 [M. G. Huber, Phys. Rev. Lett. **20**, 102 (2009) & M. G. Huber, Phys. Rev. Lett. **17**, 103 (2009)]. This revision is due to a re-analysis of the 2008 experiment that includes a more robust treatment of the phase shift caused by magnetic field gradients near the ³He cell. Furthermore, we more than doubled our original data set from 2008 by acquiring six months of additional data in 2013. Both the new data set and a re-analysis of the older data are in good agreement. Scattering lengths of low Z isotopes are valued for use in few-body nuclear effective field theories, provide important tests of modern nuclear potential models and in the case of ³He aid in the interpretation of neutron scattering from quantum liquids. The difference $\Delta b'$ was determined by measuring the relative phase shift between two incident neutron polarizations caused by the spin-dependent interaction with a polarized ³He target. The target ³He gas was sealed inside a small, flat windowed glass cell that was placed in one beam path of the interferometer. The relaxation of ³He polarization was monitored continuously with neutron transmission measurements. The neutron polarization and spin flipper efficiency were determined separately using ³He analyzers and two different polarimetry analysis methods. A summary of the measured scattering lengths for n-³He with a comparison to nucleon interaction models is given.

PACS numbers: 03.75.Dg, 28.20.Cz, 21.45.-v

Keywords: neutron interferometry, polarized ³He, few-body systems

I. INTRODUCTION

Understanding the properties of nuclei from the point of view of a collection of individual interacting nucleons is an important goal of nuclear physics [1, 2]. Unfortunately, direct calculations of low-energy nuclear phenomena using Quantum Chromodynamics (QCD) is currently impractical. Instead properties of few-body nuclear systems are calculated using a variety of phenomenological models. The prevailing two nucleon (NN) models, AV18 [3], CD-Bonn [4], and Nijmegen [5], incorporate a fit to *np* and *pp* scattering data [6] for energies up to 350 MeV. Problems arise with NN models when applying them to

systems containing more than two nucleons. This is most evident by their failure to accurately predict the binding energy of the triton by 800 keV [7]. For this reason three nucleon interactions (3N), which arise in lowest order in the meson exchange model from the exchange of two pions between three separate nucleons, are included with NN models to describe larger few-body systems. Three nucleon interactions, including Urbana [8], Tucson Melbourne [9], Brazil [10] or Illinois [7] potentials, can correct for this and now accurately predict many nuclear levels for atomic number up to 13 [7, 11, 12]. However, the increase in the prediction accuracy of binding energies has not meant that NN+3N models have accurately predicted low-energy scattering data in systems involving more than two nucleons [13, 14].

Nuclear effective field theories[15, 16] have also been a successful approach to understand few-body nuclear systems. Effective field theories separate nucleon interactions into two distinct energy regions that are separated

* michael.huber@nist.gov

[†] Also at University of Maryland, College Park, MD 20742

[‡] Also at Institute for Quantum Computing, Waterloo, ON N2L 3G1, Canada

by the pion mass. Below the pion mass threshold interaction diagrams are explicitly calculated. For higher-energy processes, the interactions are described by using low-energy observables such as scattering lengths to parameterize mean-field behavior. For instance using the triton binding energy Kirscher *et al.* [17] predicted a value of the scattering length for the singlet state in $n\text{-}^3\text{He}$ to 8 % relative uncertainty. Although presently not as precise as other approaches, effective field theories are attractive because they provide clear theoretical uncertainties from estimates of the relative contribution of higher order terms [18].

A final motivation for measuring the $n\text{-}^3\text{He}$ incoherent scattering length to high precision is that Δb also arises in the study of quantum liquids. Inelastic neutron scattering in liquid ^3He for a momentum \mathbf{Q} and energy transfer E is described by a dynamic structure factor $S(\mathbf{Q}, E)$ [19]. The dynamic structure factor can be separated into coherent S_c and incoherent S_i terms as [20, 21]

$$S(\mathbf{Q}, E) = S_c(\mathbf{Q}, E) + \frac{|\sqrt{3}\Delta b'|^2}{|b'_0 + 3b'_1|^2} S_i(\mathbf{Q}, E). \quad (1)$$

One can see that the incoherent density term is weighted by a ratio composed of both the triplet b'_1 and singlet b'_0 scattering lengths where $\Delta b' = b'_1 - b'_0$. (The real part of the scattering length is denoted by $'$). For the $n\text{-}^3\text{He}$ system the sum $b'_0 + 3b'_1$ has been previously measured to $< 1\%$ relative uncertainty. An accurate determination of $S_c(\mathbf{Q}, E)$ and $S_i(\mathbf{Q}, E)$ from $S(\mathbf{Q}, E)$ relies on determining Δb to similar precision.

Neutron scattering lengths can be determined very precisely using neutron interferometry. In the case of silicon, neutron interferometry has been utilized to measure the scattering length to 0.005 % relative uncertainty [22]. In the last few years, there have been several precision measurements using neutron interferometry with light nuclei targets. These include measurements of the spin-independent scattering length b' of $n\text{-}^1\text{H}$, $n\text{-}^2\text{H}$ [23], and $n\text{-}^3\text{He}$ [24, 25] to less than one percent relative uncertainty.

Here we report a determination of the scattering length difference $\Delta b' = b'_1 - b'_0$ of $n\text{-}^3\text{He}$ using a neutron interferometer that is based on a reanalysis of Huber *et al.* [26, 27] and additional data. A review of the relevant neutron optical theory is covered in Sec. II. The experimental setup and measured phase shift caused by the ^3He target sample is discussed in Sec. III. In Sec. IV we describe neutron polarimetry measurements using ^3He analyzers with two different analysis methods. Systematically limiting this technique is the uncertainty in the triplet absorption cross section of ^3He . This limit in determining $\Delta b'$ and other non-statistical uncertainties are discussed in Sec. V. Finally, we compare world averages of the current experimental results of the coherent and incoherent scattering lengths to various theoretical predictions in Sec. VII.

II. NEUTRON SCATTERING

Neutron scattering from a single target atom can be described by the wave function [28]

$$\Psi = e^{i\mathbf{k}\cdot\mathbf{r}} + \frac{e^{ikr}}{r} f(\theta). \quad (2)$$

The first term in Eq. (2) describes the incident neutron where \mathbf{k} is the incident wave vector and \mathbf{r} is the position of the neutron. The latter term corresponds to the scattered wave in the first Born approximation with a scattering amplitude $f(\theta)$ that can be expanded in terms of k as [29]

$$f(\theta) = -a + ika^2 + \mathcal{O}(k^2) + \dots \approx -a, \quad (3)$$

where a is called the free scattering length. The approximation in Eq. (3) is valid because the magnitude of a is of $\mathcal{O}(1\text{ fm})$ and for low energy neutrons k is of $\mathcal{O}(10^{-4}\text{ fm}^{-1})$. In general, a is complex such that $a = a' + ia''$ where a', a'' are both real numbers. As discussed later, neutron absorption by the target atom is related to the imaginary term a'' . Most importantly a represents a measurable quantity of the interaction that is unique for each nuclear isotope. In neutron interferometry, even when considering a gas target, the forward scattered momentum transfer is zero. For this reason, it is more relevant to define everything using the bound scattering length

$$b = \left(\frac{M_N + m_n}{M_N} \right) a. \quad (4)$$

Here M_N and m_n are the mass of the target atom and neutron, respectively.

To describe neutrons scattering from a homogeneous material one uses the time-independent Schrödinger equation

$$\left(\frac{\hbar^2 K^2}{2m_n} + V_{\text{opt}} \right) \psi = \frac{\hbar^2 k^2}{2m_n} \psi, \quad (5)$$

where K is the magnitude of the neutron wave vector in the material. The optical potential

$$V_{\text{opt}} = \frac{2\pi\hbar^2}{m_n} Nb, \quad (6)$$

is the effective potential of the material with an atom density N . The index of refraction

$$n = \frac{K}{k} = \sqrt{1 - \frac{\lambda^2 Nb}{\pi}}, \quad (7)$$

of the material can be derived using Eqs. (5) and (6). Here $\lambda = 2\pi/k$ is the neutron wavelength in vacuum. The index of refraction for neutron optics is conceptually the same as for light optics with two subtle differences. For one the index of refraction for neutrons is only a small

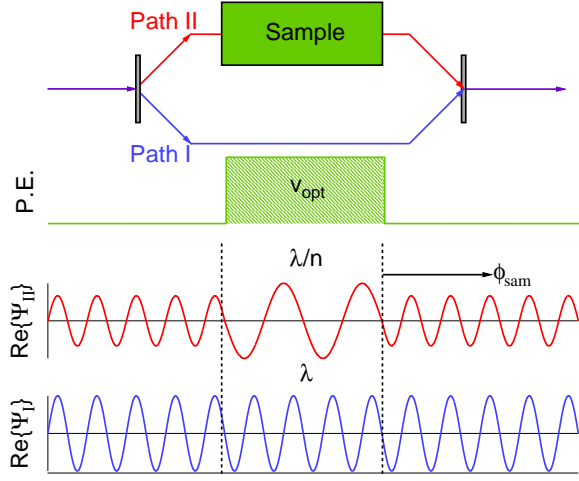


FIG. 1. A simplified schematic of an interferometer. A beam splitter separates a neutron wave function into two paths that are recombined in a final analyzing beam splitter. before being detected. A sample placed in one path causes a relative phase shift ϕ_{sam} because of a change in wavelength due to the index of refraction of the material.

deviation from unity; ie. $1 - n = \mathcal{O}(10^{-6})$ and generally n is less than one.

A neutron interferometer splits the neutron's wave function along two spatially separate paths labeled I and II. When a sample of thickness D is introduced into beam path II there is a phase difference relative to the path I of

$$\phi_{\text{sam}} = k(1 - n)D = -\lambda N D b'. \quad (8)$$

This phase shift is due to the change of the neutron wavelength as it passes through a material. A conceptual illustration of this is provided in Figure 1. A neutron interferometer is extremely sensitive to phase differences between paths and therefore can be used to measure ϕ_{sam} to high precision. Along with information of the quantities λ , N and D , often performed using individual auxiliary measurements, one can use Eq. (8) to determine the scattering length of the material.

In the case of neutrons with spin σ_n incident on a target with nuclear spin \mathbf{I} the scattering length can be written as

$$b = b_c + \frac{2b_i}{\sqrt{I(I+1)}} \sigma_n \cdot \mathbf{I}, \quad (9)$$

where b_c and b_i are called the coherent and incoherent scattering lengths, respectively. Despite its name the incoherent scattering length is due to a coherent interaction and corresponds to the spin-dependent part of the scattering length. The scattering lengths for a given spin

channel, $\mathbf{J} = \mathbf{I} \pm \sigma_n$, are defined as

$$b_+ = b_c + \sqrt{\frac{g_-}{g_+}} b_i \quad (10a)$$

$$b_- = b_c - \sqrt{\frac{g_+}{g_-}} b_i. \quad (10b)$$

Here $g_+ = (I+1)/(2I+1)$ and $g_- = 1 - g_+ = I/(2I+1)$ are statistical weight factors. Eqs. (10a) and (10b) are for general systems; for $n\text{-}^3\text{He}$ there is a triplet ($J=1$) and singlet ($J=0$) channel allowing us to write the triplet scattering length as $b_+ \equiv b_1$ and the singlet scattering length as $b_- \equiv b_0$ (likewise, $g_+ \rightarrow g_1$ and $g_- \rightarrow g_0$). Inverting Eqs. (10a) and (10b), the ^3He coherent and incoherent scattering lengths become

$$b_c = g_1 b_1 + g_0 b_0 \quad (11a)$$

$$b_i = \sqrt{g_1 g_0} (b_1 - b_0). \quad (11b)$$

The total cross section for the $n\text{-}^3\text{He}$ interaction is $\sigma_t = \sigma_s + \sigma_a$. Here σ_s is the scattering cross section given by

$$\sigma_s = \sigma_{s,c} + \sigma_{s,i} = 4\pi |b_c|^2 + 4\pi |b_i|^2. \quad (12)$$

The absorption cross section σ_a is related to the imaginary part of the scattering length b'' by the optical theorem [30]

$$\sigma_a = \frac{4\pi}{k} b''. \quad (13)$$

The measured unpolarized neutron absorption cross section for $^3\text{He}(n,p)^3\text{H}$ is $\sigma_{\text{un}} = (5333 \pm 7) \text{ b}$ [31] at the reference thermal neutron wavelength $\lambda_{\text{th}} = 1.798 \text{ \AA}$. The uncertainty quoted for σ_{un} , as well as all other uncertainties quoted below, is a standard uncertainty with a confidence level of 68 %. For $^3\text{He}(n,\gamma)^4\text{He}$ the absorption cross section is $(54 \pm 6) \mu\text{b}$ [32] at these energies and thus for our purposes can be ignored.

The absorption cross section for polarized neutrons incident on polarized ^3He nuclei is given by

$$\sigma_a = \sigma_{\text{un}} \mp P_3 \sigma_p, \quad (14)$$

where P_3 is the ^3He polarization. The \mp sign in Eq. (14) represents the cases where the neutron and ^3He spins are aligned parallel ($-$) or anti-parallel ($+$). Similar to Eqs. (11a) and (11b), σ_{un} and σ_p can be defined in terms of singlet and triplet contributions as

$$\sigma_{\text{un}} = g_1 \sigma_1 + g_0 \sigma_0 \quad (15a)$$

$$\sigma_p = g_0 (\sigma_0 - \sigma_1). \quad (15b)$$

Since σ_a is dominated by the singlet channel it is often assumed that $\sigma_1 = 0$ so that $\sigma_{\text{un}} = \sigma_p$. Although σ_1 is small there is no theoretical justification for assuming σ_1 to be precisely zero. Neutron transmission measurements are consistent with $\sigma_1 = 0$ only at the level of a few percent. The uncertainty in the triplet absorption cross section leads to the largest systematic uncertainty in both neutron interferometric and pseudomagnetic spin precision measurements of Δb . This is discussed in more detail in Section V A.

III. EXPERIMENTAL PROCEDURE

We used a neutron interferometer to measure the phase difference between two polarized neutron states that are transmitted through a polarized ^3He target cell. Neutrons are polarized in the vertical direction and can be flipped by π radians using a precession coil spin flipper. The target ^3He polarization direction stays constant throughout a measurement, but its magnitude decreases exponentially in time. For neutrons with spin state \uparrow and \downarrow incident on a polarized ^3He sample we can insert the effective scattering length for ^3He (Eq. (9))

$$b' = b'_c \pm \frac{b'_i}{\sqrt{3}}, \quad (16)$$

into Eq. (8) and find the phase difference

$$\begin{aligned} \Delta\phi_0 &= \phi_{\text{sam}}^{\uparrow} - \phi_{\text{sam}}^{\downarrow} \\ &= -\lambda N_3 D_3 \left[\left(b'_c + N_+ \frac{b'_i}{\sqrt{3}} - N_- \frac{b'_i}{\sqrt{3}} \right) \right. \\ &\quad \left. - \left(b'_c - N_+ \frac{b'_i}{\sqrt{3}} + N_- \frac{b'_i}{\sqrt{3}} \right) \right] \end{aligned} \quad (17)$$

where N_3 is the ^3He number density and D_3 is the active length of the target cell. Here $N_{\pm} = (1 \pm P_3)/2$ is the fraction of ^3He nuclei in each polarization state. Using Eqs. (11b) and (17) one finds that the phase difference between opposite neutron spin states is related to the triplet and singlet scattering lengths by

$$b'_1 - b'_0 = \frac{-2\Delta\phi_0}{N_3 \lambda D_3 P_3}, \quad (18)$$

The factors in the denominator of Eq. (18) are determined simultaneously with $\Delta\phi_0$ by measuring the spin-dependent transmission of neutrons through the ^3He cell. This is an advantage over typical interferometric measurements of b' in that none of the factors in the denominator need to be determined individually; the spin-dependent transmission asymmetry determines their product directly.

A. Neutron Interferometer and Facility

This experiment was done at the National Institute of Standards and Technology's (NIST) Center for Neutron Research (NCNR) in Gaithersburg, MD. A 20 MW reactor produces a steady source of neutrons that are moderated by a liquid hydrogen cold source [33]. These moderated neutrons are transported from the cold source to several neutron instruments by ^{58}Ni coated glass guides. At the Neutron Interferometer and Optics Facility (NIOF) a double monochromator assembly reflects 2.35 Å neutrons into an environmentally isolated enclosure [34]. The first monochromator is a single pyrolytic graphite PG(002) crystal that reflects neutrons out of the neutron guide and toward a second monochromator

3 m away. This second monochromator vertically focuses the beam using nine individually adjustable 1 cm x 5 cm PG(002) crystals [35]. Further details of the facility can be found in [36].

A schematic of the experiment inside the enclosure is shown in Figure 2. After the double monochromator assembly a pyrolytic graphite filter was used to remove $\lambda/2 = 1.175$ Å neutrons from the beam. Neutrons passing through the filter were polarized by a transmission-mode supermirror polarizer [37]. The polarizer consisted of two separate 0.64 m and 0.73 m long supermirrors that were slightly offset so that no incoming neutrons had clear line of sight to the interferometer. Neutrons in the incorrect spin state were reflected from the supermirror and absorbed on cadmium shielding.

Immediately downstream of the supermirror polarizer was a precession coil spin flipper made from two orthogonal aluminum wire coils [38]. One coil provided a magnetic field opposite of the guide field that created, in the absence of the other coil, a zero field region in the center of the coils. A second coil created a magnetic field

$$B_f = \frac{\pi^2 \hbar^2}{\mu_n m_n \lambda} L^{-1} \quad (19)$$

perpendicular to the neutron polarization direction. The field B_f was tuned such that the neutron undergoes half a Larmor precession cycle. Here L is the active length inside the coils, m_n is the neutron mass, $\mu_n = \gamma \hbar \sigma_n$ is the neutron magnetic dipole moment, and γ is the gyromagnetic ratio. When energized the precession coil spin flipper allowed the neutron spin state to be rotated π radians with nearly 100 % efficiency.

Helmholtz coils 56 cm in diameter were centered on the target cell and provided a field of 1.5 mT. To preserve the neutron polarization between the supermirror polarizer and the Helmholtz coils a series of permanent magnets provided a magnetic guide field with a minimum of 1 mT. The heat output from the Helmholtz coils, which was not actively cooled, increased the temperature variation for this experiment. The temperature around the interferometer was controlled with heating tape and calibrated platinum resistance sensors in closed loop, proportional-integral-derivative (PID) operation and typically achieved a temperature stability of ± 5 mK [35]. For this experiment the interferometer enclosure was stable to only ± 20 mK because of the increased heat caused by the Helmholtz coils.

A neutron interferometer consists of a perfect silicon crystal machined so that there are several parallel crystal blades on a common monolithic base. The interferometer used here is shown in Fig. 3. Neutrons entering the interferometer Bragg diffract in the first (splitter) blade of the interferometer. This coherently separates the neutron into two spatially separate paths labeled I and II (see Fig. 2b). Both neutron paths are Bragg diffracted in a second (mirror) blade and interfere in the final (analyzer) blade of the interferometer. Conceptually, this is analogous to a Mach-Zehnder interferometer in light

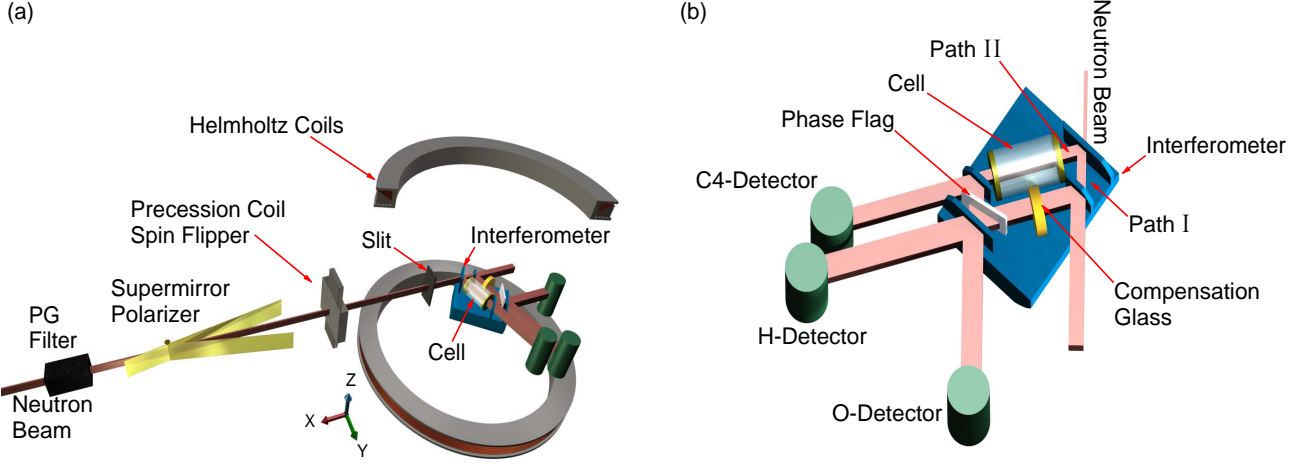


FIG. 2. The $n\text{-}^3\text{He}$ experiment (Not to Scale). (a) A monochromatic neutron beam entering from the left is polarized by a supermirror. The polarization direction can be changed using a precession coil spin flipper. A $2\text{ mm} \times 6\text{ mm}$ slit provided collimation just before the interferometer. (b) Neutrons Bragg diffract in the first blade of the interferometer coherently splitting the neutron into two separate paths. The two paths are diffracted in separate mirror blades so that they mix and interfere at the analyzer blade of the interferometer. One neutron path contains the ^3He target cell while the other path contains 8 mm of boron-free glass to compensate for the phase shift caused by the target cell windows. A quartz phase flag is rotated to vary the intensity in the two ^3He filled proportional counters labeled the O- and H-beam detectors. The ^3He polarization was monitored by a third ^3He detector labeled C4.

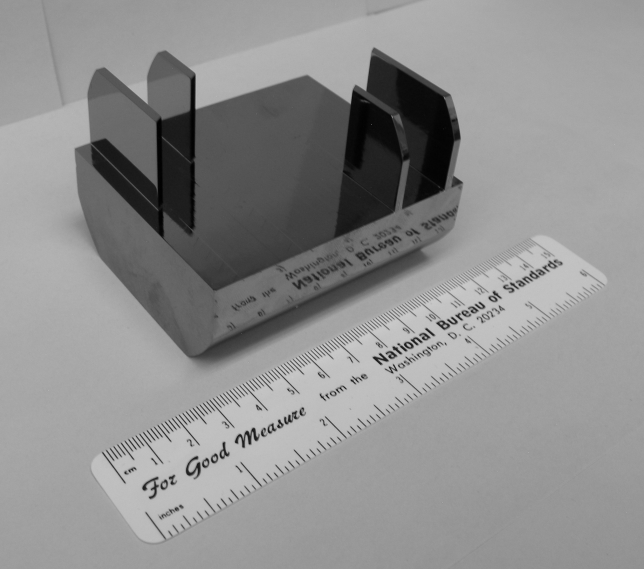


FIG. 3. The skew symmetric interferometer made by Cliff Holmes and others at the University of Missouri-Columbia machine shop (on loan from Dr. Samuel A. Werner).

optics. The two beams exiting the interferometer are historically labeled the O- and H-beams. Neutrons are detected with near 100 % efficiency using 25.4 mm diameter cylindrical ^3He filled proportional counters.

The target was a sealed glass cell containing ^3He gas (see Fig. 4) placed in path I of the interferometer. A phase flag, which consisted of 2 mm thick quartz, was

placed in both paths of the interferometer. Rotating the phase flag by an angle ϵ varied the relative phase shift between the two neutron paths and thus modulated the intensity in the O- and H-beam detectors. For the O- and H- beam detectors, the intensity can be written for a neutron with spin state \uparrow (\downarrow) as

$$I_0(\epsilon) = c_0^{\uparrow(\downarrow)} + c_1^{\uparrow(\downarrow)} \cos [\phi_{\text{flag}}(\epsilon) + \phi^{\uparrow(\downarrow)}] \quad (20)$$

$$I_H(\epsilon) = c_3^{\uparrow(\downarrow)} - c_1^{\uparrow(\downarrow)} \cos [\phi_{\text{flag}}(\epsilon) + \phi^{\uparrow(\downarrow)}] \quad (21)$$

$$\text{where } I_0 + I_H = \text{constant.} \quad (22)$$

The coefficients $c_i^{\uparrow(\downarrow)}$ for $i = 0, 1, \dots, n$ are treated as fit parameters. Here $[\phi_{\text{flag}}(\epsilon) + \phi^{\uparrow(\downarrow)}]$ is the relative phase difference between the two paths. The phase $\phi^{\uparrow(\downarrow)}$ includes both ϕ_{sam} and any initial relative phase difference between paths I and II. The term $\phi_{\text{flag}}(\epsilon) = c_2 f(\epsilon)$ is the phase shift due to the phase flag where

$$f(\epsilon) = \frac{\sin(\theta_B) \sin(\epsilon)}{\cos^2(\theta_B) - \sin^2(\epsilon)} \quad (23)$$

is the difference in optical path length for path I and II. Here $\theta_B = 37.73^\circ$ is the Bragg angle for the interferometer. Since ^3He has spin-dependent absorption, $c_i^{\uparrow} \neq c_i^{\downarrow}$ for $i = 0, 1, 3$.

The contrast or fringe visibility C of the interferometer is the ratio of the amplitude c_1 and mean c_0 in Eq. (20). In practice the contrast for a typical neutron interferometer is less than unity due to a host of reasons including small crystal imperfections and temperature gradients.

Under the best experimental conditions neutron interferometers have demonstrated at most around 90 % contrast. In this experiment there are two losses of contrast that, although not unique, are of particular interest.

The first case is due the interaction of the neutron as it passes through the glass windows of the target cell. As a neutron passes through the glass windows it experiences a large phase shift ϕ_{win} . Although this phase shift ϕ_{win} is spin-independent and is canceled when subtracting the phase measured in both neutron spin states, ϕ_{win} does affect the measured contrast and hence overall precision of the experiment. This is because the incident neutron beam contains a small wavelength spread of $\sigma_\lambda/\lambda = 1\%$. Neutrons of slightly different wavelengths will experience slightly different ϕ_{win} which dephases the detectable neutron beam after the interferometer. This doesn't affect the measured phase determined by Eq. (20) but dephasing does decrease the contrast. Assuming a Gaussian spectrum of λ , the measured contrast becomes $C = C_0 \exp[-(N_{\text{win}} D_{\text{win}} b'_{\text{win}} \sigma_\lambda)^2/2]$ where C_0 is the initial contrast of the interferometer. Here N_{win} , D_{win} , and b'_{win} are the density, thickness, and effective scattering length of the window, respectively. This effect is negligible for the ^3He itself because the density of the gas is much lower. A more complete description of coherence and subsequent contrast loss can be found in a number of sources including [35, 39–43]. To minimize the loss of contrast from the cell windows, 8 mm of compensating glass made from 2 target cell windows was placed in path I of the interferometer.

Another mechanism of contrast loss in this experiment is due to the fact that the ^3He sample is a neutron absorber; therefore both c_0 and c_1 are decreased from what they would otherwise be in an empty interferometer. For absorption we have [29],

$$c_{0'} = \frac{c_0}{2} (1 + e^{-\sigma_a N_3 D_3}) \quad (24)$$

$$c_{1'} = c_1 e^{-\sigma_a N_3 D_3/2} \quad (25)$$

$$C = \frac{c_{1'}}{c_{0'}} = C_0 \text{sech}(\sigma_a N_3 D_3/2) \quad (26)$$

Absolute contrast during this experiment was a function of the environment, effectiveness of compensation glass, neutron spin-state and the ^3He polarization and varied between 30 % and 75 %.

B. Glass Target Cells

The NIST optical shop fabricated four geometrically identical flat-windowed ^3He cells. Two of these cells, named Cashew and Pistachio (Pistachio is shown in Fig. 4) were used in this experiment. Each cell was made from boron-free aluminosilicate glass [44] and consisted of two flat 25 mm diameter, 4 mm thick windows fused onto a 34 mm long cylindrical base. Before the cells were sealed they were filled with between 1.7 bar and 1.9 bar of ^3He gas. Nitrogen and rubidium were also added in order



FIG. 4. Two ^3He cells. The larger of the two cells, called Skylight, was used in the polarimetry measurements. The smaller flat-window cell called Pistachio was used as a target cell. Rubidium deposits can be seen as dark spots along the walls of the cell.

to polarize the ^3He using spin exchange optical pumping (SEOP) [45]. Properties of the cells can be found in Table I.

The environmental constraints at the NIOF required that the cells be polarized at a separate facility. In this facility SEOP was employed to polarize the ^3He gas over a period of 2 days to an initial ^3He polarization between 65 % and 75 %. It was also possible at the SEOP facility to monitor and flip the ^3He polarization by nuclear magnetic resonance (NMR) techniques [46]. The cells were transported to the NIOF using a portable battery powered solenoid. Losses in ^3He polarization from transporting the cell between the two facilities were measured to be $< 2\%$. Helmholtz coils placed around the interferometer provided a uniform magnetic field which minimized the loss of ^3He polarization due to magnetic field gradients. Cell relaxation times at the interferometer varied per cell with a maximum of 150 h.

C. Phase Data

The phase shift caused by the spin-dependent interaction with the target ^3He was measured by rotating the phase flag from an angle of $\epsilon = 0$ mrad to ϵ_{max} and then from $\epsilon = \epsilon_{\text{min}}$ to 0 mrad in 2.18 mrad steps. The angles ϵ_{max} and ϵ_{min} varied slightly per run with $\epsilon_{\text{max}} - \epsilon_{\text{min}} = 56.68$ mrad. Each run lasted 4 h to 9 h with a statistical mode of 4.4 h. At each angle of the phase flag the

TABLE I. The ^3He cells properties. Quoted spin relaxation times are for the interferometer facility which had magnetic field gradients. $N_3\sigma_p D_3$ is the opacity of the cell. The pressure at 26 °C was determined assuming that the transmission through the cell windows was 88 % [47]. The cell Cashew's relaxation time was 135 h in 2008 and 150 h in the 2013 data set. Pistachio was used only in 2008.

Cell Name	Relaxation time [h]	$N_3\sigma_p D_3$ at 2.35 Å	Pressure [bar]	Function
Cashew ('08)	135	1.1	1.9	Target
Cashew ('13)	150	1.1	1.9	Target
Pistachio	35	1.0	1.7	Target
Skylight	110	3.1	3.1	Polarimetry
Haystack	80	3.0	2.94	Polarimetry
Whiteface	35	3.6	3.50	Polarimetry

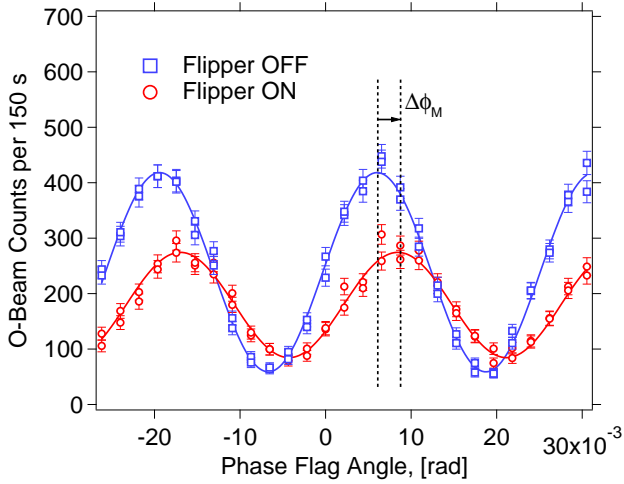


FIG. 5. Typical interferograms generated by a off-on-on-off spin flipper sequence is shown where the spin flipper is off (blue squares) and on (red circles). Each point was counted for 150 s. The lower intensity for the “Flipper ON” interferogram is due to stronger absorption in that case. The uncertainties shown are purely statistical. Lines are fits of the data using Eq. (20).

spin flipper was operated in a off-on-on-off sequence to reduce the effect of linear drifts. Two simultaneous interferograms, one for each precession coil spin flipper state, were constructed from the background subtracted off-on-on-off data. A typical pair of interferograms are shown in Fig. 5. Figure 6 shows the measured phases ϕ_1^\uparrow and ϕ_1^\downarrow over a span of a month that includes five cell transfers.

Comparing the two interferograms yields a measured phase shift $\Delta\phi_M$. A correction must be applied to $\Delta\phi_M = \phi_1^\uparrow - \phi_1^\downarrow$ in order to determine $\Delta b'$ using Eq. (18). This is because the incident beam is an incoherent mixture of both spin-up and spin-down neutrons (the neutron polarization $P_n \neq 1$). The measured interferogram

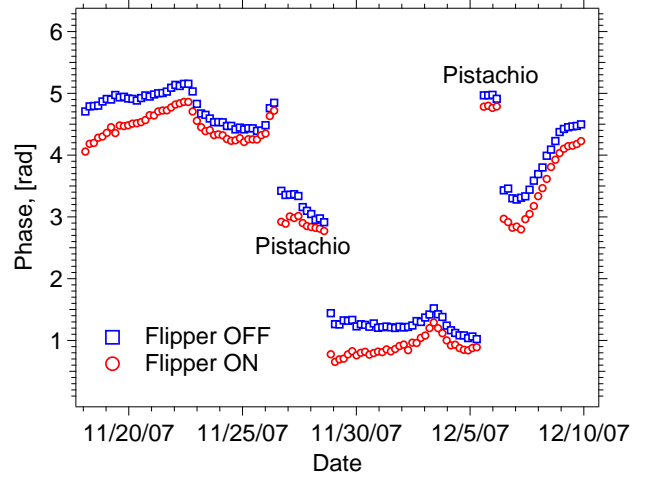


FIG. 6. The measured phases ϕ_1^\uparrow (blue squares) and ϕ_1^\downarrow (red circles) for a subset of the data that includes 5 cell transfers. The data taken with the cell Pistachio are marked. Uncertainties are smaller than the points.

is actually a sum of two different interferograms.

$$I_0(\text{off}) = c_1^\uparrow \cos(\phi_{\text{flag}} + \phi_1^\uparrow) = \cos(\phi_{\text{flag}} + \phi_2) + \eta_- \cos(\phi_{\text{flag}} + \phi_3) \quad (27)$$

where

$$\eta_- = \frac{(1 - P_n)}{(1 + P_n)} e^{-N_3\sigma_p D_3 P_3} \quad (28)$$

is the ratio of the number of minority-spin neutrons to the number of majority-spin neutrons that exit the ^3He target cell. In Eq. (27) the mean intensity has been subtracted but this does not affect the overall result below. When the precession coil spin flipper is energized

$$I_0(\text{on}) = c_1^\downarrow \cos(\phi_{\text{flag}} + \phi_1^\downarrow) = \eta_+ \cos(\phi_{\text{flag}} + \phi_2) + \cos(\phi_{\text{flag}} + \phi_3) \quad (29)$$

where

$$\eta_+ = \frac{(1 - sP_n)}{(1 + sP_n)} e^{+N_3\sigma_p D_3 P_3} \quad (30)$$

is again the ratio of the number of minority-spin to majority-spin neutrons. We can now write the measured phase shift $\Delta\phi_M$ in terms of $\Delta\phi_0 = \phi_2 - \phi_3$ which is the phase shift if the neutron polarization had been perfect (100 %) using

$$\Delta\phi_M = \arctan\left(\frac{\sin \Delta\phi_0}{\eta_+ + \cos \Delta\phi_0}\right) - \arctan\left(\frac{\eta_- \sin \Delta\phi_0}{1 + \eta_- \cos \Delta\phi_0}\right). \quad (31)$$

No correction is necessary for the fact that the helium polarization $P_3 \neq 1$ because each individual neutron interacts with multiple ^3He atoms.

We have collected two sets of $n\text{-}^3\text{He}$ phase shift data taken in separate years. The first run of this experiment done in 2008 and has previously been reported in Huber *et al.* [26, 27]. A second data set consisting of six months of additional phase measurements was taken in the spring and summer of 2013.

D. Phase shift due to a non-uniform magnetic field

When a magnetic field B in the direction of the neutron polarization is present, the additional magnetic potential $V_M = -\boldsymbol{\mu}_n \cdot \mathbf{B}$ experienced by the neutron creates a phase shift

$$\phi_{\text{mag}} = \pm \frac{\mu_n m_n \lambda D}{2\pi \hbar^2} B = \pm \kappa D B. \quad (32)$$

where $\kappa = -545 \text{ mrad}/(\text{cm}\cdot\text{mT})$. The distance D is the path length inside the interferometer. The (+) and (−) signs correspond to neutron polarization parallel and anti-parallel to the magnetic field, respectively. When calculating the phase difference between precession coil spin flipper states off and on the \pm sign in Eq. (32) reverses, hence in the absence of polarized ^3He gas this difference is $2\phi_{\text{mag}}$ for each path of the interferometer. Since the length of both interferometer paths are equal, ϕ_{mag} can only be nonzero if the magnetic field in the two paths are different. In this case, the phase shift difference will be

$$2\phi_{\text{mag}} = 2\kappa(B_1 - B_2)D \quad (33)$$

where B_1 and B_2 are the magnetic field strengths averaged over paths 1 and 2, respectively. For this interferometer the longer, parallel part of the beam paths, which contained both the cell and compensating glass, was 6.4 cm with a total path length of 8.6 cm. A magnetic field gradient will be manifested as a non-zero phase shift in the absence of polarized gas and a non-zero y-intercept for a fit of the variation of phase shift with ^3He polarization.

By direct measurements without the cell inside the interferometer Huber *et al.* [26, 27] determined $2\phi_{\text{mag}} = (2 \pm 10) \text{ mrad}$, hence consistent with zero but with a relatively large uncertainty. The fit of the phase shift data also yielded a y-intercept consistent with zero. An estimate of the gradient from the observed ^3He relaxation time in the cell Cashew yielded $2\phi_{\text{mag}} = 0.72 \text{ mrad}$ and this value was used to assign a systematic uncertainty due to magnetic field gradients. However, applying the incoherent beam correction in Eq. (31) [26] shifted the y-intercept to $(16 \pm 4) \text{ mrad}$, suggesting an underestimate of the magnetic field gradient. This led us to directly map the magnetic field, revisit the estimate from ^3He relaxation, and perform a better evaluation of the y-intercept (see Sec. VI). The need to study the effect of magnetic field gradients on the measured phase shift when $P_3 = 0$ was the leading motivation to repeat parts of the $n\text{-}^3\text{He}$

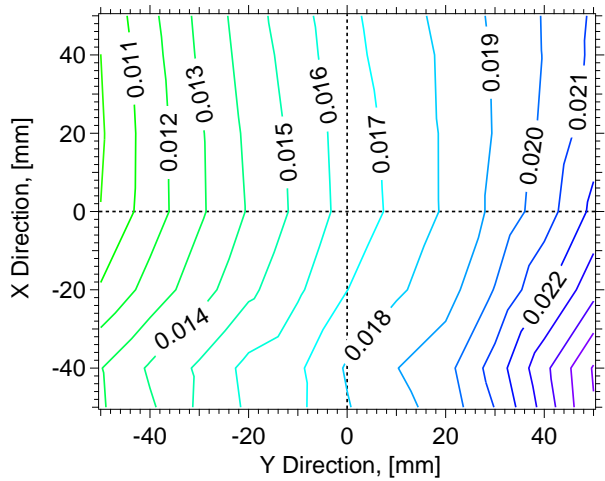


FIG. 7. The difference between the maximum magnetic field in mT and the magnetic field B_z in the region of the target cell's center (0,0) measured using a fluxgate magnetometer. Contour lines show a $7 \times 10^{-4} \text{ cm}^{-1}$ field gradient.

experiment in 2013 and revisit parts of our analysis in 2008.

Figure 7 shows a map of the magnetic field obtained with the Helmholtz coils, which revealed a fairly linear gradient $(1/B_z)dB_z/dy \approx 7 \times 10^{-4} \text{ cm}^{-1}$. The two paths of the interferometer are separated by 2.2 cm, hence this gradient yields $B_1 - B_2 \approx 2.3 \times 10^{-3} \text{ mT}$ and thus $2\phi_{\text{mag}} \approx 16 \text{ mrad}$. Although magnetic parts were avoided near the ^3He cell, there was a rotation stage with magnetic components below the coils. This stage was necessary so that the interferometer could be aligned to satisfy the Bragg condition.

The observed relaxation time T_1 of the ^3He gas results from contributions from dipole-dipole relaxation [48], wall relaxation [49], and magnetic field gradients. The first two components yield the “intrinsic” relaxation time of the cell, T_i . The observed relaxation time in the interferometer in the presence of a field gradient is

$$\frac{1}{T_1} = \frac{1}{T_i} + \frac{1}{T_{\text{fg}}} \quad (34)$$

where the gradient contribution is given by [50]

$$\begin{aligned} \frac{1}{T_{\text{fg}}} &= \frac{6700}{p} \left(\frac{|\nabla B_x|^2}{B^2} + \frac{|\nabla B_y|^2}{B^2} \right) \\ &= \frac{6700\beta^2}{p} \text{h}^{-1} \end{aligned} \quad (35)$$

Here p is the pressure in bar and $B_{x,y}$ are the perpendicular components of the magnetic field where the applied field is in the z direction. For the cell Cashew, $T_1 = 135 \text{ h}$ and $T_i = 330 \text{ h}$ which yields $\beta = 1.1 \times 10^{-3} \text{ cm}^{-1}$. Whereas β includes several components, by using $\nabla \times \mathbf{B} = 0$ and by assuming the gradient is dominated by the linear gradient observed in the field map, one obtains $(1/B_z)dB_z/dy \approx 1.0 \times 10^{-3} \text{ cm}^{-1}$, $B_1 - B_2 \approx$

3.6×10^{-3} mT and thus $2\phi_{\text{mag}} \approx 25$ mrad. It is likely that this value is an upper limit because several gradient components contribute to relaxation. As discussed in Sec. VI, we obtained y-intercepts of (16 ± 4) mrad in the 2008 run and (21 ± 3) mrad in the 2013 run, consistent with the estimates from the field map and ^3He relaxation.

Between 2008 and 2013 other interferometry experiments were performed at the NIOF. Changes to the NIOF included different shielding, changes to the polarizer, wavelength changes, the use of different interferometers and mounting, stages, and a change in the monochromator crystal [36]. Despite these changes the experimental conditions were reasonably well reproduced. Planning for additional phase data at $P_3 = 0$ was started almost immediately after 2008 as the magnetic field gradient became more of a concern. The Helmholtz coils and spin flipper were at identical positions in 2008 and 2013. Other components of the experiment like the electronics, detectors, the interferometer, cell mounting, and other system components were the same between the two runs as they were reserved for this work and not otherwise used. Initial P_3 was 10% higher in 2013 because of advances in helium polarization techniques [51]. Another difference was that in 2008 the polarization direction of P_3 was kept fixed; whereas in 2013 P_3 was twice polarized in the reversed direction. Lastly, the neutron polarization was 3% lower (see Section IV B) in 2013 due to changes in the supermirror alignment.

E. Measuring cell relaxation

Target cell transmission was measured *in situ* during each scan using the C4 detector (see Fig 8). For each run the asymmetry

$$A = \frac{I^\uparrow - I^\downarrow}{I^\uparrow + I^\downarrow} \quad (36)$$

was calculated from the individual off-on spin flipper asymmetries. The asymmetry is related to the neutron polarization P_n and spin flipper efficiency

$$s = \left| \frac{P_n(\text{on})}{P_n(\text{off})} \right|, \quad (37)$$

where on(off) refers to the state of the precession coil spin flipper [52], by

$$A = \frac{(1+s)P_n P_A}{2 + (1-s)P_n P_A}. \quad (38)$$

The values of s and P_n are known from the polarimetry measurements. For each interferogram an averaged asymmetry \bar{A} was calculated. The analyzing power P_A of a ^3He cell can be written [53]

$$P_A = \tanh(\xi) \quad (39)$$

where

$$\xi = N_3 \sigma_p D_3 P_3 \quad (40)$$

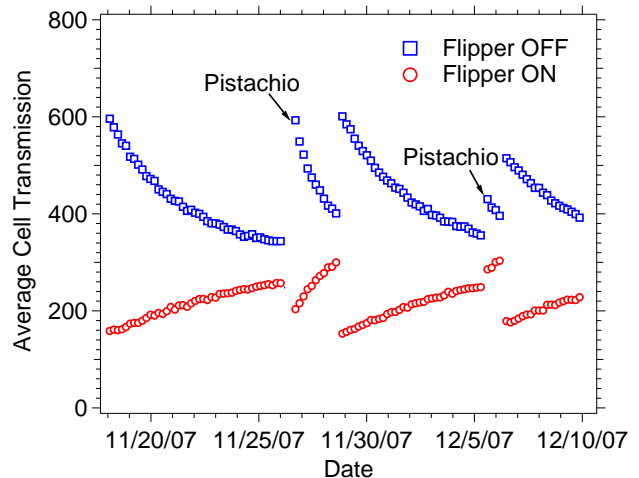


FIG. 8. The average cell transmissions I^\uparrow (blue squares) and I^\downarrow (red circles) as measured by the C4 detector for a subset of the data that includes 5 cell transfers. The data taken with the cell Pistachio are marked. Uncertainties are smaller than the points.

is the product of the opacity of the cell $N_3 \sigma_p D_3$ and ^3He polarization. One can use Eqs. (38) and (39) to write ξ in terms of the measured asymmetry \bar{A} as

$$\xi = \tanh^{-1} \left(\frac{2\bar{A}}{(s+1)P_n + (s-1)P_n \bar{A}} \right). \quad (41)$$

IV. AUXILIARY MEASUREMENTS

A. Neutron Wavelength

Because the skew symmetric interferometer uses a (220) reflection in silicon, it is necessary to eliminate higher order $n = 2, 3, \dots$ reflections from the incident beam. Neutrons with wavelengths of $\lambda < 2.35$ Å are poorly polarized by the supermirror and could potentially affect the phase and polarimetry measurements. Neutrons with wavelengths corresponding to $n \geq 3$ are suppressed by the liquid hydrogen cold source. However a non-negligible amount (5%) of $\lambda/2 = 1.175$ Å neutrons are present in the incident beam. To eliminate these neutrons a pyrolytic graphite filter [54] consisting of nine separate PG crystals of varying thickness (50 mm overall) was placed upstream of the supermirror polarizer. Neutrons of wavelength 1.175 Å are preferentially reflected by the (114) plane of the graphite and are absorbed by a surrounding boron shield.

A measurement of the fraction of $\lambda/2$ neutrons was performed with the interferometer removed and a nearly-perfect silicon analyzer crystal (NPC) placed in the direct beam before the interferometer. This crystal analyzer is denoted as “nearly-perfect” because it contains a small

mosaic spread (a small variation in lattice vector direction throughout the crystal) of 1.5×10^{-4} mrad. The mosaic of the crystal allows a greater fraction of incident neutrons to satisfy the Bragg condition; thus more reflect from the crystal and increase the overall reflected intensity. The relative intensity of $(I_{\lambda/2})/I_\lambda$ was measured by rotating the “nearly-perfect” crystal $\pm\theta_B$ and examining the reflected beams. In addition to the NPC, a disk chopper made from a rotating, neutron absorbing cadmium disk with a small slit was used as well. The disk chopper allows time-of-flight analysis of the neutron spectrum. Both techniques placed an upper limit of $(I_{\lambda/2})/I_\lambda < 0.1\%$ that was determined by comparing the relative intensities with and without the filter in place. This ratio is mainly limited by the accuracy in determining the small background signal. The presence of 1.175 \AA neutrons at this level had a negligible effect on $\Delta\phi_M$ and polarimetry measurements.

B. Polarimetry

Several neutron polarimetry measurements were made throughout the experiment to verify that the neutron polarization was stable over the duration of the experiment. Each polarimetry measurement took place during pauses in collection of the phase data. Common techniques to measure neutron polarizations and spin flipper efficiencies along with their difficulties are described in Ref. [55]. In this experiment the neutron polarization P_n was measured with ^3He cells and by using two analysis methods, which we refer to as the asymmetry and normalized transmission methods. Polarimetry cells are physically larger than target cells and one of them is shown in Fig. 4. Properties of the cells are listed in Table I.

A ^3He analyzer had two advantages over crystal or supermirror analyzers. First, the analyzing power P_A of the cell was determined from unpolarized neutron transmission measurements. Second, we could flip the cell’s polarization by π radians using nuclear magnetic resonance (NMR) at the SEOP facility. This NMR induced flip eliminated the need for a second spin flipper to uniquely determine P_n , P_A , and spin flipper efficiency. These cells had three times the opacity of the target cells and thus provided high analyzing powers that were relatively insensitive to variations in ^3He polarization.

The setup for both methods was the same. Low neutron fluence rates in the H-beam prevented any practical polarization analysis behind the interferometer. Instead, the interferometer was removed from its cradle and replaced with one of the analyzing cells. Because the neutron polarization produced by the supermirror polarizer should depend very weakly on wavelength and the beam spectrum was sufficiently narrow ($\sigma_\lambda/\lambda = 1\%$), the difference between the measured P_n of the direct beam and the neutron polarization of paths I and II of the interferometer is believed to be negligible. The neutron trans-

mission through the cell was measured using a ^3He detector located directly behind the analyzer.

For both methods the analyzing power of the cell was determined by the transmission of unpolarized neutrons. The analyzing power of a ^3He cell is given by Eq. (39). For the polarimetry cells the range of initial P_A was between 86 % and 99 % but was typically around 97 % depending on the cell and its initial ^3He polarization. Eq. (39) can be rewritten as a ratio of two unpolarized neutron transmission measurements as

$$P_A = \sqrt{1 - \left(\frac{T_{\text{un}}}{T_{\text{pol}}}\right)^2} \quad (42)$$

where $T_{\text{pol}}(T_{\text{un}})$ is the transmission of unpolarized neutrons through a polarized (unpolarized) ^3He cell. These transmissions are discussed later in Sec. IV B 2. Unpolarized neutrons were obtained by translating the supermirror out of the beam using an encoded linear stage. The position of the supermirror was reproducible to within $1 \mu\text{m}$. To measure T_{un} the analyzer cell was depolarized by temporarily connecting the Helmholtz coils to an alternating current voltage supply.

1. Asymmetry Method

The asymmetry method used the difference in count rates for the two neutron spin states, I^\uparrow and I^\downarrow , to determine the neutron polarization and spin flipper efficiency. Here $I^{\uparrow(\downarrow)}$ is the intensity when the neutron and ^3He polarization are aligned parallel (anti-parallel). The asymmetry A is related to the neutron polarization and spin flipper efficiency by

$$A = \frac{I^\uparrow - I^\downarrow}{I^\uparrow + I^\downarrow} = \frac{(1+s)P_n P_A}{2 + (1-s)P_n P_A}. \quad (43)$$

To uniquely determine P_n and s using this method it is necessary to have two separate asymmetries A and A^* where one reverses the direction of the ^3He polarization. Similar to Eq. (43) we have

$$A^* = \frac{(1+s)P_n P_{A^*}}{2 - (1-s)P_n P_{A^*}} \quad (44)$$

The analyzing powers P_A and P_{A^*} were not the same because of a few percent loss in P_3 caused by performing an NMR induced spin flip and transporting the cell to and from the SEOP facility. Using Eqs. (43) and (44) the spin flipper efficiency is

$$s = \frac{A[1+A^*]P_{A^*} + P_A[A-1]A^*}{A[A^*-1]P_{A^*} + P_A[1+A]A^*}. \quad (45)$$

With knowledge of s , P_n can be determined via

$$\begin{aligned} P_n &= \frac{2A}{P_A[(s-1)A + (1+s)]} \\ &= \frac{2A^*}{P_{A^*}[(1-s)A^* + (1+s)]}. \end{aligned} \quad (46)$$

Measurements of P_n and s that were obtained using the asymmetry method are shown in Fig. 9.

The intensities I^\uparrow and I^\downarrow for both this method and normalized transmission method discussed in Section IV B 2 were performed symmetrically around measurements of T_{pol} and hence P_A and P_{A^*} . Specifically, I^\uparrow (and likewise I^\downarrow) was measured twice, once before and once after a measurement of T_{pol} . The averages of I^\uparrow and I^\downarrow were then used in Eqs. (43) and (44). This was done to compensate for the decay of P_3 while the measurements were being performed to a level where no correction for P_3 decay was needed.

2. Normalized Transmission Method

When $P_n = 1$ the transmission of neutrons through a polarized ^3He cell is

$$\begin{aligned} T_{\text{off(on)}} &= T_g \exp(-N_3 \sigma_a D_3) \\ &= T_g \exp(-N_3 \sigma_{\text{un}} D_3) \exp(\pm \xi), \end{aligned} \quad (47)$$

where Eqs. (14) and (40) have been used to relate the absorption cross section σ_a to ξ . The signs (+) and (-) is for ‘off’ and ‘on’ states of the precession coil spin flipper, respectively. Here we have taken that the initial neutron polarization and ^3He polarization is in the same direction. T_g is the transmission of neutrons through the cell windows.

For a neutron beam with $P_n \leq 1$ the transmission T_{off} becomes

$$\begin{aligned} T_{\text{off}} &= \left(\frac{T_g}{2} \right) e^{-N_3 \sigma_{\text{un}} D_3} \\ &\times \left[(1 + P_n) e^\xi + (1 - P_n) e^{-\xi} \right]. \end{aligned} \quad (48)$$

Eq. (48) can be expressed more compactly as

$$T_{\text{off}} = T_g e^{-N_3 \sigma_{\text{un}} D_3} [\cosh(\xi) + P_n \sinh(\xi)]. \quad (49)$$

The transmission of unpolarized neutrons through a polarized ^3He cell is given by

$$T_{\text{pol}} = T_{\text{un}} \cosh(\xi), \quad (50)$$

where

$$T_{\text{un}} = T_g e^{-N_3 \sigma_{\text{un}} D_3} \quad (51)$$

is the transmission of unpolarized neutrons through an unpolarized ^3He cell. Dividing Eq. (49) by Eq. (50) yields

$$\frac{T_{\text{off}}}{T_{\text{pol}}} = 1 + P_n \tanh(\xi). \quad (52)$$

It follows from Eqs. (39), (42), and (52) that

$$P_n = \frac{\frac{T_{\text{off}}}{T_{\text{pol}}} - 1}{\sqrt{1 - \left(\frac{T_{\text{un}}}{T_{\text{pol}}} \right)^2}}. \quad (53)$$

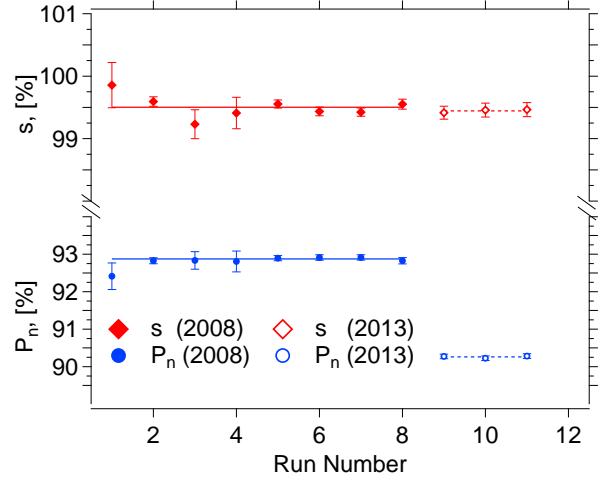


FIG. 9. The neutron polarization (circles) and spin flipper efficiency (diamonds) measured in 2008 (solid) and 2013 (open) determined using the asymmetry method. The uncertainties shown are purely statistical. Fits of the data are shown as solid lines for 2008 and dotted lines for 2013. Points with larger uncertainties were taken when the cell had lower polarization.

When one energizes the spin flipper one has the anti-parallel case where,

$$sP_n = \frac{1 - \frac{T_{\text{on}}}{T_{\text{un}}}}{\sqrt{1 - \left(\frac{T_{\text{un}}}{T_{\text{pol}}} \right)^2}}. \quad (54)$$

It should be noted that the uncertainty associated with determining the polarimetry from Eq. (53) is different than that for Eq. (54). Propagating the uncertainty σ of the polarization product $Z_{\text{off}} = P_A P_n$ and $Z_{\text{on}} = P_A s P_n$ we find

$$\sigma_{Z_{\text{off}}}^2 = \left(\frac{1}{T_{\text{un}}} \right)^2 \sigma_{T_{\text{off}}}^2 + \left(\frac{T_{\text{off}}}{T_{\text{un}}^2} \right)^2 \sigma_{T_{\text{un}}}^2 \quad (55)$$

$$\sigma_{Z_{\text{on}}}^2 = \left(\frac{1}{T_{\text{un}}} \right)^2 \sigma_{T_{\text{on}}}^2 + \left(\frac{T_{\text{on}}}{T_{\text{un}}^2} \right)^2 \sigma_{T_{\text{un}}}^2. \quad (56)$$

For this experiment $Z_{\text{off}} \approx Z_{\text{on}} \approx 0.9$ and $T_{\text{on}} \approx 0.05 T_{\text{off}}$. Using Eqs. (55) and (56) we find that

$$\sigma_{Z_{\text{on}}} \approx 0.05 \sigma_{Z_{\text{off}}}. \quad (57)$$

So despite the relative uncertainties of T_{off} and T_{on} being comparable the overall uncertainty in determining P_n versus sP_n differs by a factor of twenty. The contribution to the overall uncertainty of P_n from the uncertainty in P_A is small because of higher statistics without the supermirror in the neutron beam. By reversing the ^3He spin using NMR we can invert Eq. (57) so that

$$\sigma_{Z_{\text{off}}} \approx 0.05 \sigma_{Z_{\text{on}}} \quad (58)$$

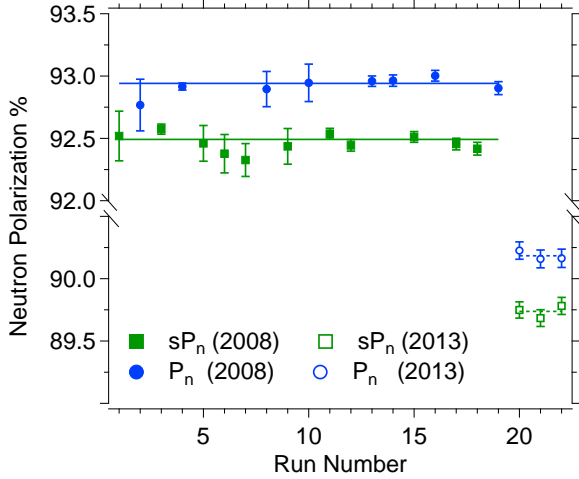


FIG. 10. The neutron polarization (circles) and neutron polarization when energizing the precession coil spin flipper (squares) measured in 2008 (solid) and 2013 (open) determined using the normalized transmission method. The uncertainties shown are purely statistical. All points shown were taken in the anti-parallel state of n - ^3He (see text). Fits of the data are shown as solid lines for 2008 and dotted lines for 2013. Points with larger uncertainties were taken when the cell had lower polarization.

when the ^3He polarization has been flipped. It follows that using the anti-parallel state to determine P_n or sP_n is advantageous despite a much smaller $T_{\text{off(on)}}$ being measured because the overall uncertainty is better. Thus we have chosen to use only the anti-parallel measurements for the normalized transmission method (shown in Figure 10).

3. Polarimetry Result

Both the asymmetry and normalized transmission methods yield neutron polarizations and spin flipper efficiencies to less than 0.1 % relative standard uncertainty. These results are shown in Table II. For the 2008 data set there was a 2σ disagreement in measured neutron polarization between the two methods. To handle this discrepancy, the uncertainties for the 2008 polarimetry results are determined by adding the largest uncertainty of the two methods in quadrature with the difference between the methods, for example $\sigma_{P_n} = \sqrt{\sigma_{\text{largest}}^2 + (\Delta P_n)^2} = \sqrt{(0.0033)^2 + (0.92874 - 0.92941)^2}$. In 2013 the polarimetry (see Figs. 9 and 10) data were more consistent and this expansion of their uncertainty was not done. An equal weighted average of the asymmetry and normalized transmission methods yields

$$\begin{aligned} P_n &= 0.92908 \pm 0.00075 \quad \text{in 2008} \\ &= 0.90227 \pm 0.00055 \quad \text{in 2013} \end{aligned} \quad (59)$$

TABLE II. Results of the polarimetry for the various methods used. σ_R is the relative standard uncertainty.

Var.	Method	2008		2013	
		Value (σ)	σ_R , [%]	Value (σ)	σ_R , [%]
P_n	Asy.	0.92874(33)	0.04	0.90260(36)	0.04
	N.T.	0.92941(17)	0.02	0.90184(41)	0.05
	Asy. + N.T.	0.92908(75)	0.09	0.90227(55)	0.06
s	Asy.	0.99502(31)	0.03	0.99444(63)	0.06
	N.T.	0.99516(23)	0.02	0.99506(63)	0.06
	Asy. + N.T.	0.99510(34)	0.03	0.99475(89)	0.09

and

$$\begin{aligned} s &= 0.99510 \pm 0.00034 \quad \text{in 2008} \\ &= 0.99475 \pm 0.00089 \quad \text{in 2013} \end{aligned} \quad (60)$$

The differences between the 2008 and 2013 neutron polarization is believed to be due to non-reproducible changes in the angular separation between the two mirror surfaces of the supermirror polarizer that is often varied between experiments. In both 2008 and 2013 the neutron precession coil spin flipper was the same device, was located in the same place, and showed much better agreement.

V. SYSTEMATIC EFFECTS

A. Absorption Cross Section

The quantity ξ is a function of λ and can be written as

$$\xi = N_3 \sigma_p D_3 P_3 = N_3 \left[\frac{1}{4} (\sigma_0 - \sigma_1) \right] \frac{\lambda}{\lambda_{\text{th}}} D_3 P_3, \quad (61)$$

where $\lambda_{\text{th}} = 1.798 \text{ \AA}$ is the reference thermal neutron wavelength. To extract $N_3 \lambda D_3 P_3$ from ξ , one needs the singlet and triplet absorption cross sections σ_0 and σ_1 . The experimental value of $\sigma_{\text{un}} \approx \sigma_0/4$ is well known from transmission measurements as $(5333 \pm 7) \text{ b}$ at λ_{th} [31]. However, the triplet absorption cross section is poorly known experimentally. Passell and Schermer [56] measured neutron transmission through ^3He and determined the ratio of singlet to total absorption cross section to be $g_0 \sigma_0 / \sigma_{\text{un}} = (1.010 \pm 0.032)$. An indirect measurement of the same quantity was made by Borzakov *et al.* [57] where they determined $g_0 \sigma_0 / \sigma_{\text{un}} = (0.998 \pm 0.010)$ by examining deviations from a purely “ $1/v$ ” absorption law for neutron energies up to 150 keV. Both of these experiments support $\sigma_1 \approx 0$ but only at the 1 % level. Due to the lack of precision measurements of σ_1 , we used a theoretical prediction of the imaginary part of the scattering length to estimate σ_1 .

Calculations performed by Hofmann and Hale [58, 59] of the imaginary free scattering length a'_1 using R-matrix

and AV18+3N interactions give a range of values a_1'' of between 0.0012 fm and 0.0051 fm. However as noted in the same paper, AV18+3N models under-predict the experimentally measured a_0'' by up to 30 %. To be conservative we used $a_1'' = (0.005 \pm 0.005)$ fm. This allowed for the possibility that theoretical calculations are low by as much as a factor of two. With a_1'' and the measured thermal absorption cross section for unpolarized ^3He we have

$$\sigma_0 - \sigma_1 = (21236 \pm 100) \text{ b.} \quad (62)$$

With Eqs. (41) and (62) one may extract $N_3\lambda D_3 P_3$ from the asymmetry measurements of ξ .

B. Polarimetry Effects

The effect of uncertainties in P_n and s on calculating $\Delta\phi_0$ is complicated by the fact that they affect both η_- and η_+ directly and also indirectly through ξ . To determine the systematic uncertainty in $\Delta\phi_0$ contributed by the uncertainties σ_{P_n} and σ_s we studied a simulated set of $[\Delta\phi_M]_{\text{sim}}$ and $[\xi]_{\text{sim}}$ data. This simulated data was generated using a fixed value $\Delta b' = -5.400$ fm and a randomly distributed set of $[\xi]_{\text{sim}}$ to generate a $[\Delta\phi_M]_{\text{sim}}$. $\Delta\phi_0$ was then calculated using the simulated $[\Delta\phi_M]_{\text{sim}}$ and $[\xi]_{\text{sim}}$ while varying P_n and s by their respective uncertainties. The variance in $\Delta\phi_0$, and hence $\Delta b'$, resulting from the uncertainties σ_{P_n} and σ_s was taken as the systematic uncertainty due to the polarimetry measurements.

VI. RESULTS

Figure VI shows the measured $\Delta\phi_0$ versus ξ for the 2008 data set which was collected over several reactor cycles for a total of 12 weeks. From Eq. (18) the value of $\Delta b'$ can be determined by the slope of $\Delta\phi_0$ in Figure VI. There are two significant changes in determining $\Delta b'$ from what was done previously in Huber *et al.* [26, 27]. The first and most significant is that in Huber *et al.* the slope of $\Delta\phi_0$ versus ξ was determined using a one parameter fit. This fixed the y-intercept of the fit to be precisely zero corresponding to $\Delta\phi_0 = 0$ at $P_3 = 0$. In the presence of a magnetic field gradient, this approach is no longer valid. Instead we now perform a two parameter fit of $\Delta\phi_0$ versus ξ . The fitted y-intercept of the data shown in Fig. VI yields $2\phi_{\text{mag}} = (16 \pm 4)$ mrad.

The other change we have made has been in the manner in which we cut individual data points. In Huber *et al.* we cut the data based on the reduced chi squared χ_{red}^2 of the interferogram fit. All fits with $\chi_{\text{red}}^2 \geq 1.5$ were discarded and not included in our 2008 results. This was done to account for phase instabilities especially those seen immediately following a cell transfer which introduced temporary temperature and mechanical instabilities lasting 12 h or more. However, discarding interferograms based on χ_{red}^2 values included eliminating points

taken in the middle of runs where the phase was more stable. As discussed below, a systematic uncertainty of 0.012 fm attributed to phase instabilities was also applied to the result in Huber *et al.* Since we already incorporate an uncertainty due to phase instabilities, for this result we make no cut based on the χ_{red}^2 in either the 2008 or 2013 data set. Phase instabilities were greater in 2013 as the temperature stability that we had in 2008 was not reproduced. This is contrary to 2008 where temperature drifts were highly correlated to opening the facility doors to perform a cell transfer (since $P_3 \approx 0$ in most of 2013, transfers were infrequent in that data run). The inclusion of data points with $\chi_{\text{red}}^2 \geq 1.5$ does not affect the values determined by a fit of $\Delta\phi_0$ versus ξ but does decrease the statistical uncertainty.

A two parameter fit of Fig. VI gives $\Delta b' = (-5.381 \pm 0.053)$ fm with $\chi^2/d.o.f. = 530/(435 - 2) = 1.2$. This χ^2 represents a low probability of fit ($< 1\%$) and is due to random phase instabilities that were most likely caused by small temperature fluctuations. To estimate the systematic uncertainty due to this effect the uncertainty of $\Delta\phi_0$ was inflated by 0.016 rad in quadrature with the statistical uncertainty for each point so that the $\chi^2/d.o.f. = 1$. The average statistical uncertainty for $\Delta\phi_0$ was ≈ 0.033 rad but varied strongly with P_3 . A histogram of the residual of the fit with a reduced $\chi^2 = 1$ is shown in the inset of Fig. VI. The distribution of points in the figure closely follows a Gaussian function centered at zero.

Figure VI shows $\Delta\phi_0$ versus ξ for the 2013 data set. In 2013 we polarized the ^3He gas only four times focusing instead on measuring $\Delta\phi_0$ at low P_3 . Twice we polarized the ^3He in the opposite direction with respect to the neutron polarization defined by the super-mirror polarizer. In this case there is more neutron absorption when the precession coil spin flipper is off. This reversed-polarized data is shown in the lower left quadrant of Fig. VI. Again applying a two parameter fit of Fig. VI gives $\Delta b' = (-5.439 \pm 0.038)$ fm with a $\chi^2/d.o.f. = 1120/(507 - 2) = 2.2$. To fix $\chi^2/d.o.f. = 1$ the uncertainty of $\Delta\phi_0$ was inflated in quadrature by 0.043 rad. For 2013 we find that $2\phi_{\text{mag}} = (21 \pm 3)$ mrad which is consistent with both the 2008 data and the field gradient measurement.

The weighted average of both data sets gives

$$\Delta b' = (-5.411 \pm 0.031 \text{ (Stat.)} \pm 0.039 \text{ (Syst.)}) \text{ fm.} \quad (63)$$

The uncertainty budget for $\Delta b'$ is given in Table III. The weighted average is performed by weighting both the statistical and systematic uncertainties unrelated to neutron absorption on ^3He in quadrature. The systematic uncertainty related to ^3He absorption was added to the total systematic uncertainty in Eq. (63).

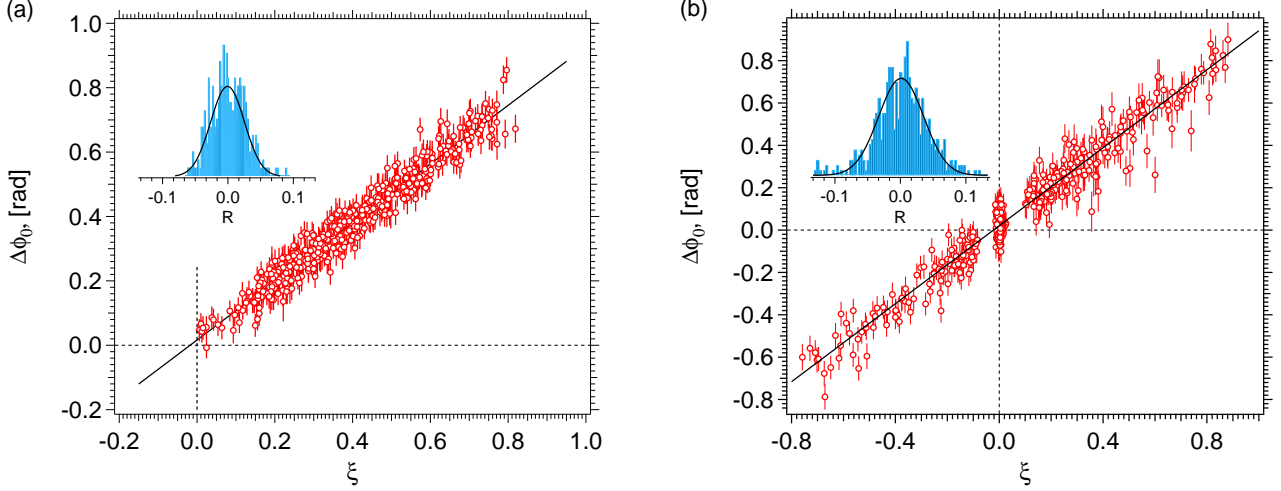


FIG. 11. $\Delta\phi_0$ vs ξ values for (a) 2008 and (b) 2013. The solid line is a weighted average with a $\chi^2/d.o.f. = 1$ (see text). Insets: Histograms of the residual distribution with Gaussian fits (solid lines). The residual is defined by $R = y_i - y$ where y is the fit function and y_i is the i^{th} data point. (a) The Gaussian fit is centered at -0.001 rad with a full width half maximum (FWHM) of 0.091 rad. (b) The Gaussian fit is centered at $+0.002$ rad with FWHM of 0.117 rad.

TABLE III. The uncertainty budget for $\Delta b'$. Uncertainties related to ^3He absorption cross section that are identical for both data sets are summed in quadrature.

2008		2013
σ , [fm]	Parameter	σ , [fm]
0.053	$\Delta\phi_0/\xi$ Fit (Statistical)	0.038
0.028	Triplet absorption cross section σ_1	0.028
0.007	Total absorption cross section σ_{un}	0.007
0.029	Total systematic from cross sections	0.029
0.025	Phase instabilities	0.040
0.005	Neutron polarization P_n	0.004
0.002	Spin flipper efficiency s	0.004
0.026	Total non-cross section systematic	0.040
0.053	Total statistical	0.038
0.039	Total systematic	0.049

VII. CONCLUSIONS AND DISCUSSION

We have performed a precision measurement of the difference $\Delta b' = (-5.411 \pm 0.031 \text{ (Stat.)} \pm 0.039 \text{ (Syst.)})$ fm between the triplet and singlet scattering lengths of $n\text{-}^3\text{He}$ using neutron interferometry to 0.9% relative standard uncertainty. The ultimate precision of this technique is systematically limited by the triplet absorption cross section corresponding to a relative uncertainty of 0.5%. This result is in good agreement with the only previous direct measurement of $\Delta b' = (-5.462 \pm 0.046)$ fm performed by Zimmer *et al.* at the Institut Laue-Langevin (ILL) [60]. Ref. [60] used a spin echo apparatus to measure the relative difference in the pseudo-magnetic spin-precession [61, 62] between a neutron pass-

ing though a polarized ^3He cell compared to an empty reference beam. That technique is fundamentally different than the technique applied here. One can state the results independent of the triplet absorption cross section and total absorption cross section from our results and that of Ref. [60]. This is done for two reasons: (i) both groups estimated σ_1 differently and (ii) in the event of future more accurate measurements of the absorption cross sections, one can immediately update the spin-dependent $n\text{-}^3\text{He}$ scattering length. Zimmer *et al.* determined σ_1 from a average of the experimental results of Refs. [56] and [57] with the limitation that $\sigma_1 \geq 0$. Whereas, as described in Section V A, we used a theoretically predicted σ_1 but with an inflated uncertainty. Our result stated independent of the triplet absorption cross section is

$$\Delta b'(\text{this work}) = \left[(-10.1929 \pm 0.0760) \times 10^{-4} \text{ fm/b} \right] \times \left(1 - \frac{\sigma_1}{\sigma_{\text{un}}} \right) \sigma_{\text{un}} \quad (64)$$

This is in disagreement with the result of Zimmer *et al.* of

$$\Delta b'(\text{Ref. [60]}) = \left[(-10.3628 \pm 0.0180) \times 10^{-4} \text{ fm/b} \right] \times \left(1 - \frac{\sigma_1}{\sigma_{\text{un}}} \right) \sigma_{\text{un}} \quad (65)$$

by 2σ when factoring out the absorption cross sections.

There have been a number of experiments measuring the coherent scattering length of $n\text{-}^3\text{He}$ defined by Eq. (11a) using techniques such as measuring neutron

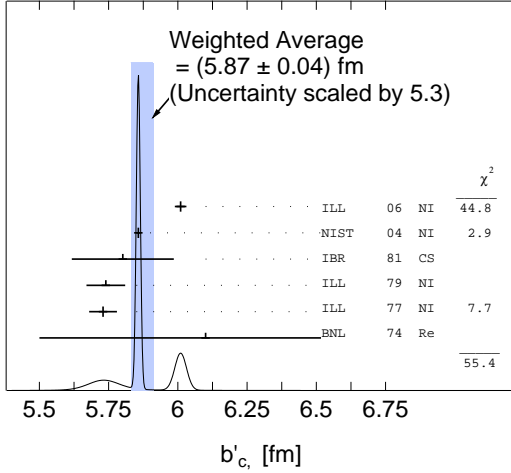


FIG. 12. An ideogram of the coherent scattering length measurements for n - ^3He taken from Refs. [24, 25, 63–66]. The blue band represents the weighted average $\pm\sigma$ of the three experiments with smallest quoted uncertainties. Techniques used were neutron interferometry (NI), total cross section (CS), and reflectivity (RE).

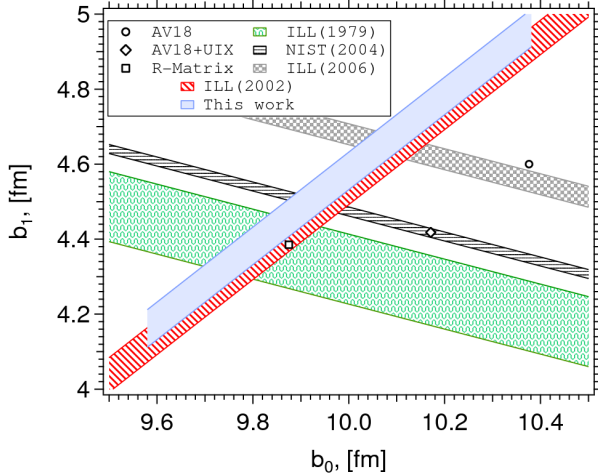


FIG. 13. Current experimental data on the n - ^3He system from this work, ILL 2006 [25], NIST 2004 [24], ILL 2002 [60], ILL 1979 [65] compared to theoretical predictions [58, 59]. Bands represent the experimentally determined values $\pm 1\sigma$.

reflectivity, relative phase shifts, and neutron transmissions. The three most precise measurements of b'_c were done with neutron interferometry; Kaiser *et al.* [64], Huffman *et al.* [24], and Ketter *et al.* [25]. However, the two most recent results differ by more than 7σ . Figure 12 shows an ideogram of the coherent scattering length measurements. Each measurement is represented by a Gaus-

sian centered about their result with a normalized area equal to $1/\sigma$ [67]. The uncertainty of the weighted average has been inflated in the manner described in Ref. [67].

Calculations employing models AV18+UIX, AV18+UIX+ V_3^* [58, 59], and AV18+LL2 [17] have all predicted similar values for the triplet and singlet scattering lengths. For example $\Delta b'(AV18 + UIX) = (-5.753 \pm 0.002)\text{fm}$. Neither this work nor the work of Zimmer *et al.* agrees with NN+3N calculations. Figure 13 shows a selection of measured values of b_1 and b_0 beside some theoretical predictions. Four nucleon interactions have yet to be included into the theoretical models due to the difficulty in handling long-range Coulomb forces, but should constitute only a tiny correction to NN + 3N predictions. A calculation of pion-less effective field theory to Next to Leading Order (NLO) shows promise [17], but the uncertainty of the predicted value is still too large to compare to high-precision measurements. A recent measurement of the total scattering cross section [68] that suggests a much larger scattering cross section and would lie outside of Fig. 13 is omitted for space.

The recent work on the n - ^3He interaction can lead to further understanding of low energy nucleon systems. Although there are several discrepant measurements, scattering length measurements do not match theoretical models. Taken alone, the coherent scattering length by [24] agrees with AV18+UIX, but doesn't intersect a measurement of the spin-dependent difference in triplet and singlet states. This work and [60] agrees with the R-matrix prediction. More work needs to be done to resolve the discrepancy between different n - ^3He coherent scattering length measurements. The uncertainty in the triplet absorption cross section needs to be experimentally determined to better precision, if other measurements of the spin-dependent quantity $\Delta b'$ are to be made. The authors hope that this work along with the previous scattering length measurements can improve future NN+3N models, and is part of the ongoing exploration into few-body systems at the NIOF.

ACKNOWLEDGMENTS

We wish to thank John Fuller and Jeff Anderson at NIST for making the glass target cells. The development and application of the polarized ^3He cells and methods used in this experiment was supported in part by the Department of Energy, Basic Energy Sciences. Also we would like to thank Sam Werner and Helmut Kaiser for their helpful discussions. This work is supported by NIST and the National Science Foundation through grants PHY-0555347, PHY-0855445, and PHY-1205342.

[1] R. Lazauskas, J. Carbonell, A. C. Fonseca, M. Viviani, A. Kievsky, and S. Rosati, Phys. Rev. **C71**, 034004

(2005).

- [2] M. Viviani, A. Kievsky, L. Marcucci, and S. Rosati, Nucl. Phys. **A751**, 226 (2005).
- [3] R. B. Wiringa, V. G. J. Stoks, and R. Schiavilla, Phys. Rev. **C51**, 38 (1995).
- [4] R. Machleidt, Phys. Rev. **C63**, 024001 (2001).
- [5] V. G. J. Stoks, R. A. M. Klomp, C. P. F. Terheggen, and J. J. de Swart, Phys. Rev. **C49**, 2950 (1994).
- [6] V. G. J. Stoks, R. A. M. Klomp, M. C. M. Rentmeester, and J. J. de Swart, Phys. Rev. **C48**, 792 (1993).
- [7] S. C. Pieper, V. R. Pandharipande, R. B. Wiringa, and J. Carlson, Phys. Rev. **C64**, 014001 (2001).
- [8] B. S. Pudliner, V. R. Pandharipande, J. Carlson, S. C. Pieper, and R. B. Wiringa, Phys. Rev. **C56**, 1720 (1997).
- [9] S. A. Coon, M. D. Scadron, P. C. McNamee, B. R. Barrett, D. W. E. Blatt, and B. H. J. McKellar, Nucl. Phys. **A317**, 242 (1979).
- [10] M. R. Robilotta and H. T. Coelho, Nucl. Phys. **A460**, 645 (1986).
- [11] R. B. Wiringa, R. Schiavilla, S. C. Pieper, and J. Carlson, Phys. Rev. C **89**, 024305 (2014).
- [12] R. B. Wiringa and S. C. Pieper, Phys. Rev. Lett. **89**, 182501 (2002).
- [13] M. Viviani, A. Kievsky, S. Rosati, E. A. George, and L. D. Knutson, Phys. Rev. Lett. **86**, 3739 (2001).
- [14] T. C. Black, P. R. Huffman, D. L. Jacobson, W. M. Snow, K. Schoen, M. Arif, H. Kaiser, S. K. Lamoreaux, and S. A. Werner, Phys. Rev. Lett. **90**, 192502 (2003).
- [15] E. Epelbaum, A. Nogga, W. Glöckle, H. Kamada, U.-G. Meißner, and H. Witala, Phys. Rev. **C66**, 064001 (2002).
- [16] D. R. Entem and R. Machleidt, Phys. Rev. **C68**, 041001 (2003).
- [17] J. Kirscher, H. W. Griesshammer, D. Shukla, and H. M. Hofmann, “Universal Correlations in Pion-less EFT with the Resonating Group Model: Three, and Four Nucleons,” (2009), arXiv:0909.5606 [nucl-th].
- [18] P. F. Bedaque, H. W. Hammer, and U. van Kolck, Nucl. Phys. **A646**, 444 (1999).
- [19] H. R. Glyde, *Excitations in Liquid and Solid Helium* (Oxford University Press, 1995).
- [20] K. Sköld, C. A. Pelizzari, R. Kleb, and G. E. Ostrowski, Phys. Rev. Lett. **37**, 842 (1976).
- [21] H. R. Glyde, B. Fåk, N. H. v. Dijk, H. Godfrin, K. Guckelsberger, and R. Scherm, Phys. Rev. **B61**, 1421 (2000).
- [22] A. Ioffe, D. L. Jacobson, M. Arif, M. Vrana, S. A. Werner, P. Fischer, G. L. Greene, and F. Mezei, Phys. Rev. **A58**, 1475 (1998).
- [23] K. Schoen, D. L. Jacobson, M. Arif, P. R. Huffman, T. C. Black, W. M. Snow, S. K. Lamoreaux, H. Kaiser, and S. A. Werner, Phys. Rev. **C67**, 044005 (2003).
- [24] P. R. Huffman, D. L. Jacobson, K. Schoen, M. Arif, T. C. Black, W. M. Snow, and S. A. Werner, Phys. Rev. **C70**, 014004 (2004).
- [25] W. Ketter, W. Heil, G. Badurek, M. Baron, E. Jericha, R. Loidl, and H. Rauch, Euro. Phys. J. **A27**, 243 (2006).
- [26] M. G. Huber, M. Arif, T. C. Black, W. C. Chen, T. R. Gentile, D. S. Hussey, D. A. Pushin, F. E. Wietfeldt, and L. Yang, Physical Review Letters **103**, 179903 (2009).
- [27] M. G. Huber, M. Arif, T. C. Black, W. C. Chen, T. R. Gentile, D. S. Hussey, D. A. Pushin, F. E. Wietfeldt, and L. Yang, Physical Review Letters **102**, 200401 (2009).
- [28] M. L. Goldberger and F. Seitz, Phys. Rev. **71**, 294 (1947).
- [29] V. F. Sears, *Neutron Optics* (Oxford University Press, 1989).
- [30] E. Feenberg, Phys. Rev. **40**, 40 (1932).
- [31] S. F. Mughabghab, *Atlas of Neutron Resonances: Resonance Parameters and Thermal Cross Sections Z=1-100* (Elsevier, 2006).
- [32] F. L. H. Wolfs, S. J. Freedman, J. E. Nelson, M. S. Dewey, and G. L. Greene, Phys. Rev. Lett. **63**, 2721 (1989).
- [33] R. E. Williams and J. M. Rowe, Physica **B311**, 117 (2002).
- [34] M. Arif, D. E. Brown, G. L. Greene, R. Clothier, and K. Littrell, Vib. Monit. Cont. **2264**, 20 (1994).
- [35] D. A. Pushin, M. Arif, M. G. Huber, and D. G. Cory, Phys. Rev. Lett. **100**, 250404 (2008).
- [36] M. G. Huber, D. Pushin, and C. B. Shahi, Nuclear Instruments & Methods (2014 In preparation).
- [37] A. Ioffe, P. Fischer, T. Krist, and F. Mezei, J. Phys. Soc. Jap. Suppl. **A65**, 80 (1996).
- [38] G. Badurek, H. Rauch, A. Zeilinger, W. Bauspiess, and U. Bonse, Phys. Lett. **A56**, 244 (1976).
- [39] R. Clothier, H. Kaiser, S. A. Werner, H. Rauch, and H. Wöhlwitsch, Phys. Rev. **A44**, 5357 (1991).
- [40] H. Kaiser, S. A. Werner, and E. A. George, Phys. Rev. Lett. **50**, 560 (1983).
- [41] A. G. Klein, G. I. Opat, and W. A. Hamilton, Phys. Rev. Lett. **50**, 563 (1983).
- [42] D. Petrascheck, Physica **B151**, 171 (1988).
- [43] H. Rauch, H. Wöhlwitsch, H. Kaiser, R. Clothier, and S. A. Werner, Phys. Rev. **A53**, 902 (1996).
- [44] T. R. Gentile and J. Fuller, J. Amer. Glass. Soc. , 21 (2007).
- [45] T. G. Walker and W. Happer, Rev. Mod. Phys. **69**, 629 (1997).
- [46] F. Bloch, Phys. Rev. **70**, 460 (1946).
- [47] T. Chupp *et al.*, Nuclear Instruments and Methods **A574**, 500 (2007).
- [48] N. R. Newbury, A. S. Barton, G. D. Cates, W. Happer, and H. Middleton, Phys. Rev. A **48**, 4411 (1993).
- [49] W. A. Fitzsimmons, L. L. Tankersley, and G. K. Walters, Phys. Rev. **179**, 156 (1969).
- [50] J. W. McIver, R. Erwin, W. C. Chen, and T. R. Gentile, Review of Scientific Instruments **80**, 063905 (2009).
- [51] W. C. Chen, T. R. Gentile, Q. Ye, T. G. Walker, and E. Babcock, Journal of Applied Physics **116**, 014903 (2014).
- [52] A. R. Wildes, Rev. Sci. Inst. **70**, 4241 (1999).
- [53] D. R. Rich *et al.*, Nucl. Inst. Meth. **A481**, 431 (2002).
- [54] G. Shirane and V. J. Minkiewicz, Nucl. Inst. Meth. **89**, 109 (1970).
- [55] B. G. Yerozolimsky, Nucl. Inst. Met. **A420**, 232 (1999).
- [56] L. Passell and R. I. Schermer, Phys. Rev. **150**, 146 (1966).
- [57] S. Borzakov, H. Malecki, L. Pikelnier, M. Stempinski, and E. Sharapov, Sov. J. Nucl. Phys. **35**, 307 (1982).
- [58] H. M. Hofmann and G. M. Hale, Phys. Rev. **C68**, 021002 (2003).
- [59] H. M. Hofmann and G. M. Hale, Phys. Rev. **C77**, 044002 (2008).
- [60] O. Zimmer, G. Ehlers, B. Farago, H. Humblot, W. Ketter, and R. Scherm, Euro. Phys. J. **4**, 1 (2002).
- [61] V. B. Baryshevsky and M. I. Podgoretsky, JETP **20**, 704 (1965).
- [62] A. Abragam, G. L. Bacchella, H. Glätti, P. Meriel, M. Pinot, and J. Piesvaux, Phys. Rev. Lett. **31**, 776 (1973).
- [63] T. A. Kitchens, T. Oversluizen, L. Passell, and R. I. Schermer, Phys. Rev. Lett. **32**, 791 (1974).
- [64] H. Kaiser, H. Rauch, W. Bauspiess, and U. Bonse, Phys.

- Lett. **71**, 321 (1977).
- [65] H. Kaiser, H. Rauch, G. Badurek, W. Bauspiess, and U. Bonse, Physik **A291**, 231 (1979).
- [66] V. Alfimenkov, S. B. Borzakov, V. V. Tkhan, A. Govorov, L. Lason, L. Pikel'ner, and E. Sharapov, Sov. J. Nucl. Phys. **33**, 467 (1981).
- [67] C. Amsler *et al.*, Phys. Lett. **B667** (2008).
- [68] K. Guckelsberger, W. Nistler, R. Scherm, and M. Weyrauch, Physica **B276-B278**, 975 (2000).